PCCP

ROYAL SOCIETY OF CHEMISTRY

PAPER

View Article Online
View Journal | View Issue

Cite this: *Phys. Chem. Chem. Phys.*, 2021, **23**, 3071

Hydrogen abstraction/addition reactions in soot surface growth†

Qingzhao Chu, [ab] Baolu Shi, [b] Hongyu Wang, [a] Dongping Chen*[a] and Lijuan Liao*[c]

Received 11th December 2020,
Accepted 28th December 2020

DOI: 10.1039/d0cp06406h

rsc.li/pccp

The hydrogen abstraction (HB) and addition reactions (HD) by H radicals are examined on a series of polycyclic aromatic hydrocarbon (PAH) monomers and models of quasi-surfaces using quasi-classical trajectory (QCT) method. QCT results reproduce the rate constants of HB reactions on PAH monomers from density functional theory (DFT) in the range of 1500–2700 K. The PAH size has a minor impact on the rates of HB reactions, especially at temperatures beyond 2100 K. In contrast, HD reactions have a clear size dependence, and a larger PAH yields a higher rate. It was also found that the preferred reaction pathway changes from HB to HD reactions at ~1900 K. The rates of surface HB and HD reactions exceed those in the gas phase by nearly one factor of magnitude. Further analysis of the detailed trajectory of the QCT method reveals that about 50% of surface reactions can be attributed to the events of surface diffusion, which depends on the local energy transfer in gas-surface interactions. However, this phenomenon is not preferred in PAH monomers, as expected. Our finding here questions the treatment of the surface reactions of soot as the product of the first collision between the gaseous species and particle surface. The surface diffusion-induced reactions should be accounted for in the rates of the surface HB and HD reactions. The rate constants of HB and HD reactions on each reactive site (surface zig-zag, surface free-edge and pocket free-edge sites) were calculated by QCT method, and are recommended for the further development of surface chemistry models in soot formation.

1. Introduction

Soot particles have attracted intensive public attention due to their hazardous effects on the environment and human health.[1] Soot formation involves the chemistry of precursors, particle nucleation and mass/size growth.[2] The surface reactions of soot play an important role in its mass growth, involving interactions between gaseous species and active sites on particle surface. Thus, the influence of the surface structure on its reactivity is critical to infer the mass growth of soot.

Polycyclic aromatic hydrocarbons (PAHs) are accepted as the precursors of soot and also as its main building block.[3,4] Many experimental investigations and chemical kinetic model studies have been performed on PAHs to understand the mechanism in soot surface reactions.[5,6] Since the calculations of reactions involving large aromatic molecules are quite time-consuming, it is well established to infer the reaction pathways and rate constants of large hydrocarbons using smaller species *via* the rate-rule assumption. Transition state theory (TST) is one of the most common methods for estimating rate constants. A series of studies using the TST approach have been conducted to examine the effect of the PAH size on the reactivity. Hou *et al.*[7] computed the energetics of hydrogen abstraction from benzene and naphthalene using the method of density functional theory (DFT), and they found that M06-2X/6-311G(d,p) has the best performance with errors within 1 kcal mol^{-1} compared to the CCSD(T)/CBS calculations. It was also revealed that the effects of PAH sizes, structures, and reaction sites on the rate constants of hydrogen abstraction reactions are limited from benzene to pentacene due to the similar energy barriers. Liu *et al.*[8] reported that the hydrogen-abstraction/acetylene-addition (HACA) reactions are sensitive to the site type. According to the local structure, reactive sites are divided into three types, *i.e.*, free-edge, zig-zag and armchair site. Among all three site types, the free-edge site is the most reactive one. For hydrogen abstraction reactions, it was found that the difference in the energy barrier over all site types is less than 1 kcal mol^{-1}, and the obvious deviation (*e.g.*, ~41%) in rate constants is attributed to the effect of orientation hindrance, where the reactive site is hindered by the local geometry. Semenikhin and coworkers performed a systematic study on

[a] *State Key Lab of Explosion Science and Technology, Beijing Institute of Technology, Beijing, 100081, China. E-mail: dc516@bit.edu.cn*
[b] *School of Aerospace Engineering, Beijing Institute of Technology, Beijing, 100081, China*
[c] *Key Laboratory for Mechanics in Fluid Solid Coupling Systems, Institute of Mechanics, Chinese Academy of Sciences, Beijing, 100190, China. E-mail: liaohuanxin@hotmail.com*

† Electronic supplementary information (ESI) available. See DOI: 10.1039/d0cp06406h

H abstraction from benzo(*a*)pyrene and chrysene molecules using B3LYP/6-31G(d) and G3 theories. They found that zig-zag sites appear to be more reactive than armchair sites (37–42%).[9] They further applied these rate constants to model the surface oxidation, and successfully reproduced the experimental results of the shock-initiated oxidation of soot.[10] As discussed above, TST method can predict accurate rate constants for the PAH molecules up to pentacene, but this method becomes too expensive for large PAHs and soot particles.

The surface HACA model developed by Frenklach and coworkers[11] has been widely applied to address the mass growth due to surface reactions. In this model, the rate of the surface reaction (R_s) is determined by $R_s = \alpha\chi_i A_s R_g$, where α is an empirical parameter accounting for the probability of a gaseous molecule colliding with the reactive sites on particle surface, χ_i is the number density of the reactive site i, A_s is the particle surface area, and R_g is the reaction rate of an analogous gas-phase reaction. The R_g was adapted from the hydrogen abstraction on benzene according to the rate-rule assumption, and the activation energy barrier was lowered by 3 kcal mol^{-1} based on the assumption that the reactive C–H sites are located at the aromatic bay.[12] Although the reduced activation energy barrier was recently confirmed from high-level quantum calculations,[9] this approximation might not be applicable for all situations. Therefore, an alternative method is required to examine the site effect and quantify the surface reaction rates. However, the available experimental methods are not able to extract the surface reactivity of soot at the atomic level. Recently, molecular dynamics (MD) simulations have become popular in the research of soot formation, for instance, soot particle inception[13,14] and the morphology evolution[15] of soot particles. Chen *et al.*[16] successfully built microscopic structures of PAH clusters to mimic soot particles, and managed to estimate the surface properties, including the surface area, number density of reactive sites and parameter α. They also found that the surface shallow regions (*e.g.*, pockets) are frequently formed owing to the surface rearrangement of PAH molecules.[17] It was speculated that the reactivity of the reactive site in the pocket region is different from its counterpart; however, this has not been further investigated in detail.

Besides the TST and MD methods, the quasi-classical trajectory (QCT) is an alternative method using classical mechanics to describe the collision between a target molecule and a collision partner,[18] and is widely applied to extract the rate constants of bimolecular reactions in the gas phase.[19–21] Compared to the TST method, the QCT method examines the detailed characteristics of collision and energy transfer with a higher computing cost. Song *et al.* applied the QCT method to study the dynamics of the H atom colliding with the diamond {111} surface. They observed a phenomenon termed the ''mobile transition state'', where an incident species bounces around the surface sites before forming a covalent bond.[22] Fu *et al.*[23] reported a high-level computational study of roaming dynamics in the bimolecular combustion reaction, H + C_2H_4 = H_2 + C_2H_3. It was learnt that the binary collision can lead to ''collision-induced'' roaming, *i.e.*, the incident H radical roams over the C_2H_4 molecule before a hydrogen abstraction reaction occurs. This unique behavior is an important contributor in the overall reaction rate, but it cannot be accessed by any conventional minimum-energy path (*e.g.*, TST approach). In the study of the soot surface reactions, Frenklach and Mebel recently proposed a mechanism of rotationally-induced formation of E-bridges to interpret the nucleation in soot growth,[24,25] while no direct work is available in the soot surface reaction, and this motivates us to explore the collision dynamics of the surface hydrogen abstraction and addition reactions using QCT method.

In this paper, potential collisions between the incident species and soot surface were explored using the QCT method to reveal the detailed dynamics of surface reactions in soot formation. First, molecular structures are analyzed to obtain the solvent-excluded surface (SES) area and percentages of the surface hydrogen. The detailed collision dynamics are then extracted from the quasi-classical trajectories to analyze the collision cross sections and reaction rate constants. Furthermore, the local properties of each site, including the per-site SES area, available incident angle, and local van der Waals potential energy surface, are discussed to illustrate the site effects on the collision dynamics. The detailed dynamics of the surface reactions are examined to identify the impact of gas-surface scattering. Finally, the rate constants of the hydrogen abstraction and addition reactions on each site are recommended for soot surface models.

2. Computational methods

2.1 Quasi-classical trajectory

Two representative models are selected in this work to reveal the collision dynamics of hydrogen atoms with polycyclic aromatic hydrocarbons. We first consider the PAH monomers of benzene (A1), coronene (A7), and circumcoronene (A19) to mimic the interactions between the H atoms in gaseous reactions. Two quasi-surface configurations are further constructed using both A7 and A19, termed as A7s and A19s. The selection of the PAH size is based on the recent studies of mass spectra[26] and high-resolution atomic force microscopy[27] in sooting flames, indicating that soot particles are composed of PAHs with a mass ranging from 100 to 700 amu.

QCT calculations were performed using the above two models to compare the dynamics of hydrogen abstraction/addition reactions on PAH monomers (Fig. 1a) and the soot surface (Fig. 1b). As shown in Fig. 1a, a PAH monomer was placed in the box center. The initial orientation and vibrational energy of the PAH monomers were randomly sampled from the equilibrium configuration at the corresponding temperature. The initial distance between the H atom and the center of mass (COM) of the PAH monomers is defined as $d = \sqrt{x^2 + b^2}$, where x is set to 35 Å and $b = \xi^{1/2} b_{max}$ is the impact parameter.[28] ξ is a random number that follows a uniform distribution in (0,1), and b_{max} is the maximum impact factor in the sampling process, which is 6 Å, 8.5 Å and 10.5 Å for A1, A7 and A19, respectively. The initial velocity of H atoms in the x direction was sampled from the Maxwell–Boltzmann distribution at the sampled temperature, while the velocity components in both y and z directions were set to 0.

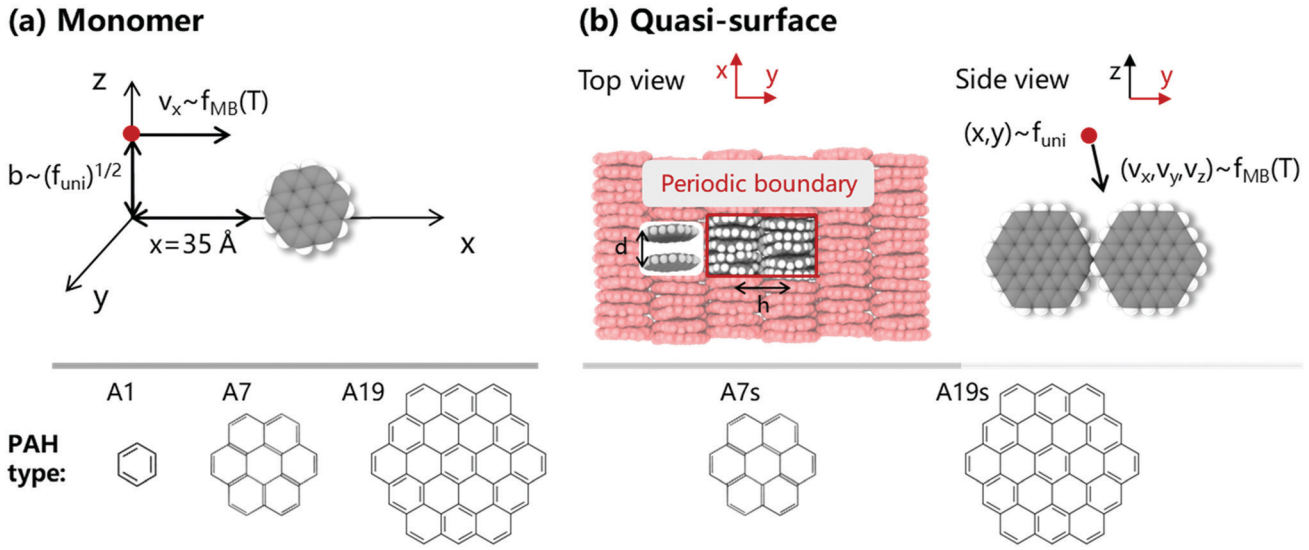

Fig. 1 The initial configurations of the quasi-classic trajectories for the (a) PAH monomers and (b) PAH quasi-surfaces. Periodic boundary conditions are applied to the *x*- and *y*-directions of the PAH quasi-surface, and ghost molecules are represented by a red color (top view in the left panel of (b)). $f_{MB}(T)$ and f_{uni} represent the sampling from the Maxwell–Boltzmann distribution and uniform distribution, respectively. *d* and *h* refer to the layer separation and distance between the PAH stacks of the minimum unit in the models of the quasi-surfaces.

The second model represents the quasi-surface of soot particles. As shown in the left panel of Fig. 1b, the quasi-surface is composed of A7 or A19 monomers, and the minimum unit contains two columns of PAH stacks, which is built from five monomers. Periodic boundary conditions were applied to both *x*- and *y*-directions. In the current configurations, the surface hydrogen atoms are exposed to the gas species from the *z*-direction without carbon-rich regions. This is consistent with the geometry of nascent soot particles.[29,30] To guarantee the initial configurations sitting at the potential minimum (see Fig. S1 in the ESI†), parameter *d* was set as 3.3 Å for A7s and A19s, and the values *h* of A7s and A19s were 10.2 and 15.1 Å, respectively (Fig. 1b). A bottom restraint was added to the lowest (in *z*-direction) layer of atoms to avoid the surface evaporation at high temperatures and improve the sample efficiency. The bottom restraint is a common method in the studies of the metal surface reactions.[31,32] Prior to production simulations, the potential impact of the bottom restraint was carefully examined in Fig. S2 (ESI†). The bottom restraint causes negligible impacts on the reaction probabilities and kinetic energy transfer.

The initial setup of the QCT simulations using the quasi-surfaces (Fig. 1b) is different from that of the PAH monomers. An H atom was placed 20 Å above the surface, and the *x*- and *y*-positions were both randomly sampled. The initial *x*-, *y*- and *z*-velocity components of the H atom were randomly assigned from a Gaussian distribution. However, the speed distribution followed the Maxwell–Boltzmann distribution at the sampled temperature. These randomly sampled *x*-, *y*-, *z*-components of the incident velocity ensure that the incident angle covers the range of 0° to 180°. In addition, the surface temperature was consistent with the sampled temperature.

A temperature range of 1500–2700 K was selected to cover the flame conditions.[33] In this work, the temperature controls two main parameters, *i.e.*, the relative velocity of the incident H atom and the vibrational energies of the PAH monomers and quasi-surfaces. The Nose–Hoover thermostat was applied for the system equilibration (*i.e.*, 10 ps), and the *NVE* ensemble was used for further QCT simulations. At each temperature, the total number of trajectories was 6000 and 3000 for each PAH monomer and quasi-surface, respectively. The selected numbers of trajectories were statistically sound to sample the reactivity of these configurations (Fig. S3, ESI†). In total, 168 000 QCT simulations were conducted to reveal the reaction kinetics on the PAH monomers and quasi-surfaces. All of the trajectories were integrated using a time step of 0.2 fs for a maximum time of 10 ps, and the system energy is conserved (Fig. S4, ESI†). If the COM distance of two fragments exceeds 40 Å, the trajectory is truncated to avoid unnecessary calculations. All of the MD simulations are carried out using a LAMMPS simulator.[34]

The collision cross section between the H atom and PAH monomers can be written as:

$$\sigma_{\mathrm{mono,H}} = \pi {b_{\mathrm{mac}}}^2 \quad (1)$$

The collision cross section between the H atom and quasi-surface ($\sigma_{\mathrm{surf,H}}$) is calculated by the geometric area of the quasi-surface, which are 358.05 Å^2 and 514.91 Å^2 for A7s and A19s, respectively. The reaction probability is defined as:

$$P_{\mathrm{r}} = \frac{N_{\mathrm{r}}}{N_{\mathrm{total}}}, \quad (2)$$

where N_{r} and N_{total} are the number of reactions and total trajectories, respectively. The rate constant at the temperature *T* is then calculated by:

$$k(T) = \langle v_{\mathrm{r}} \rangle \sigma P_{\mathrm{r}} \quad (3)$$

with the mean collision velocity:

$$\langle v_r \rangle = \left(\frac{8k_B T}{\pi\mu}\right)^{\frac{1}{2}}, \quad (4)$$

where k_B is the Boltzmann constant and μ is the reduced mass of reactants. The fraction of the reaction on a reactive site i is defined as the ratio of the reaction events on site i ($N_{r,i}$) to the total reaction events (N_r) at a temperature T,

$$f_i(T) = \frac{N_{r,i}}{N_r}. \quad (5)$$

We can further define the per-site rate constant of site i as:

$$k_i(T) = f_i(T)k(T). \quad (6)$$

It should be noted that the QCT method is based on a binary collision assumption, where the incident H atom does not interact with other species during the sampling time (t = 10 ps). At a high pressure, the binary collision assumption might fail, and the interactions between the incident species should be considered. The critical pressure can be estimated by the sampling time and the area of the reactive site. A detailed discussion can be found in the ESI.† For current systems at 2000 K, the QCT sampling method is applicable for pressures lower than 23.1 atm.

2.2 Force field validation

The potential energy surface of the PAH systems was explored using reactive molecular dynamics. We selected the ReaxFF force field to describe the interactions between the carbon and hydrogen atoms, and the parameters were taken from Mao *et al.*,[13,35] which has been widely used to describe the nucleation and growth of the incipient soot particles. The ReaxFF parameters have been validated by the binding energy of the PAH dimers against the M06-2X/def2SVP level of theory.[36] To further examine the accuracy of the ReaxFF force field on the collision dynamics between PAH and H atom, the intermolecular potential energy for benzene and H atom were calculated by the ReaxFF force field and a DFT method, that is, B3LYP-D3/6-311++G(d,p). Several data points from the calculations of CCSD(T)/cc-pVTZ are also added for reference. In Fig. 2, the energy curves are presented for four orientations. It was found that the results of the ReaxFF force field are in good agreement with those using the B3LYP-D3/6-311++G(d,p) method. Compared with the CCSD(T)/cc-pVTZ method, both ReaxFF and B3LYP-D3/6-311++G(d,p) methods overestimate the potential well depth by ~0.43 kcal mol^{-1} at the maximum. An unexpected fluctuation of around 3.3 Å exists in the prediction of the ReaxFF force field in Fig. 2d. This indicates a potential issue in the original parameterization of the ReaxFF force field, but the fluctuation is less than 0.2 kcal mol^{-1} and does not influence the collision dynamics of the H atom with PAHs in this study. Besides the intermolecular potential energies, the reaction energy barrier of the hydrogen abstraction from benzene was also studied in Fig. S5 (ESI†). DFT calculations at the M06-2X/6-311G(d,p) and B3LYP/6-31G(d) level of theory are compared with that using the ReaxFF force field. There is good agreement between the ReaxFF force field and M06-2X/6-311G(d,p) results,

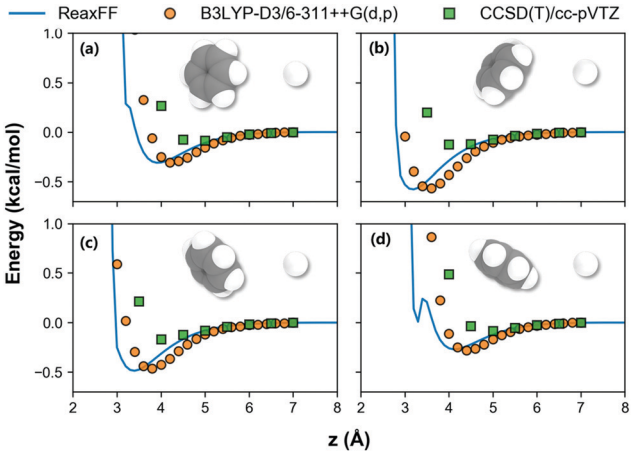

Fig. 2 Intermolecular energy curves of a benzene with an H atom calculated from the methods of the ReaxFF force field, B3LYP-D3/6-311++G(d,p) and CCSD(T)/cc-pVTZ.

and the error for the reaction energy barrier is less than 1 kcal mol^{-1}. More importantly, the ReaxFF force field is ~150 000 times faster than the DFT method at the M06-2X/def2SVP level of theory,[36] which enables the simulations of the quasi-surface models.

2.3 Post-process methods

A solvent-excluded surface (SES) was used to evaluate the surface properties of the PAH monomers and quasi-surfaces. This approach has been applied to investigate the surface reactivity of soot.[16,17] The SES area was calculated by the MSMS 6.2.1 program[37] using a "rolling ball" algorithm. The radii of the carbon and hydrogen atoms were taken from their van der Waals radii as 1.7 Å and 1.2 Å, respectively.[38] The probe size was taken from the radius of the hydrogen atom. For each case, 200 equilibrium structures were sampled from trajectories over 10 ps at a specific temperature to calculate the mean and standard deviation values of the SES area. In addition, the MSMS program has been updated to adapt periodic boundary conditions for the quasi-surface cases.

The collisions between atoms were determined by the van de Waals radii. The incident H atom can react with both C and H atoms on target configurations. A homemade code was developed to recognize the bond formation by the atomic distance and duration. If the distance of two atoms, *i.e.*, r, is shorter than the critical value r_{crit} and the duration exceeds t_{crit}, these two atoms are considered as "bonded". A detailed analysis has been performed to examine the effects of r_{crit} and t_{crit} on the predicted bonded information (Fig. S6, ESI†). As a result, r_{crit} and t_{crit} are 1.2 Å and 0.2 ps for the C–H bonds, respectively. In contrast, we selected r_{crit} = 1.0 Å and t_{crit} = 0.2 ps for the H–H bonds. The selected r_{crit} values of the C–H and H–H bonds are comparable to their bond length in typical molecules. The bond length of the C–H bond in C_6H_6 is 1.083 Å (calculated at the CCSD(T)/cc-pVTZ level of theory),[39] and the bond length of the H–H bond in H_2 is 0.743 Å. Considering the bond vibrations at high temperatures, r_{crit} is longer than the bond length, as expected. The bootstrapping resampling method[40] was used to extract error bars in our

calculations. The sample size and the number of repeats were adapted as 3000 and 20, respectively (Fig. S7, ESI†).

3. Results and discussion

3.1 Molecule structures

Table 1 lists the surface properties of the PAH monomers and quasi-surfaces at 1500 and 2700 K. The percentage of the surface hydrogen is defined as $\alpha_H = A_H/A_{total}$, where A_H and A_{total} are the SES area of the hydrogen atom and all surface sites, respectively. The α_H also refers to the probability of a successful collision on the surface H atoms. It should be noted that both A_{SES} and α_H present weak dependence on the temperature, for example, the A_{SES} of A19s increases by only $\sim$2% when changing temperature from 1500 to 2700 K. At 1500 K, A1 yields the largest α_H as 0.49, while the α_H of A19 is only 0.29. This change can be attributed to the increase in the C/H ratio from A1 to A19. As shown in Fig. 1b, the current configurations of the quasi-surface models represent a hydrogen-rich surface as the surface H atoms point outward, resulting in a large α_H as $\sim$0.80 at 1500 K, and the difference between A7s and A19s is minor, *i.e.*, 0.02–0.03. The equivalent collision radius $R_{c,SES}$ of PAH monomers can be calculated from the SES area assuming spherical molecules, $R_{c,SES} = \sqrt{A_{SES}/(4\pi)} + R_H$, where R_H is the van der Waals radius of the hydrogen atom as 1.2 Å. The geometrical radius R_{geo} is extracted from the optimized structure at the M06-2X/6-311G(d,p) level of theory. The $R_{c,geo}$ is calculated as:

$$R_{c,geo} = d_{H,COM} + R_H, \quad (7)$$

where $d_{H,COM}$ represents the distance between the farthest H atom in a PAH to the COM. As Table 1 shows, $R_{c,geo}$ values are always higher than $R_{c,SES}$. Increasing the PAH size, the discrepancy between $R_{c,geo}$ and $R_{c,SES}$ increases from $\sim$0.78 to 2.12 Å.

Table 1 Surface properties of all considered configurations at 1500 and 2700 K

Case	T (K)	A_{SES} (Å^2)	α_H	$R_{c,SES}$ (Å)	$R_{c,geo}$[a] (Å)
A1	1500	106.03	0.49	2.90	3.68
	2700	108.61	0.49	2.94	—
A7	1500	273.38	0.38	4.66	5.99
	2700	275.44	0.36	4.68	—
A19	1500	496.38	0.29	6.28	8.40
	2700	502.77	0.28	6.33	—
A7s	1500	475.72[b]	0.79	—	—
	2700	471.26[b]	0.75	—	—
A19s	1500	767.03[b]	0.82	—	—
	2700	786.52[b]	0.77	—	—

[a] $R_{c,geo}$ values were calculated using the optimized structure at the M06-2X/6-311G(d,p) level of theory. [b] The top surface of the minimum unit is reported here.

3.2 Collision dynamics

PAH molecules are usually planar species,[27] and the collision between the PAH molecule and gaseous species depends on the relative orientation and velocity. We first examine the effect of orientation. Fig. 3a shows that the impact factor reaches the maximum value (b_{max}) when the relative velocity is perpendicular to the plane of the PAH molecules. When the relative velocity is parallel to the plane, the impact factor decreases to its minimum value. The collision status of all A1 trajectories is plotted in Fig. 3b. All 7 temperature cases from 1500 to 2700 K, *i.e.*, 42 000 trajectories, are included, and the collision status is tagged as "Collide" and "Miss". Clearly, all incident H atoms collide on PAHs when $b < 3$ Å, and the proportion of the "Collide" trajectories gradually decreases from 1 to 0 when 3 Å $< b <$ 6 Å. In this transition region, the relative orientation between the PAH molecule and H atom determines the collision dynamics. The relative velocity of H and PAH has a minor impact on the calculated collision probability (P_{coll}) from 1500 to 2700 K due to the weak van der Waals potential (Fig. S8, ESI†). It was reported that collisions between large particles at high temperatures could cause a significant reduction in the impact factor.[41] However, in this work, the potential between the PAH monomer and H atom is relatively weak and causes negligible impacts on collision events. The P_{coll} values of A7 and A19 are included in Fig. S9 (ESI†), which are consistent with that of A1 (Fig. 3b). The collision radius from the MD trajectories ($R_{c,MD}$) can be calculated using:

$$R_{c,MD} = \left(\int_0^{b_{max}} 2bP_{coll}(b)db\right)^{\frac{1}{2}}. \quad (8)$$

The derivation of $R_{c,MD}$ is included in the ESI.† Fig. 3c shows that $R_{c,MD}$ is independent of the system temperature, but

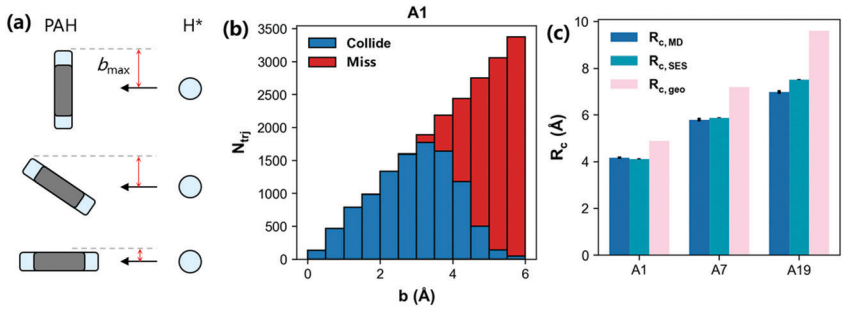

Fig. 3 (a) Illustration of the impact factor in different orientations. (b) The status of the collision trajectories between A1 and the incoming H atom with different impact factors. (c) The effective collision radius calculated by MD trajectories ($R_{c,MD}$), SES area ($R_{c,SES}$) and geometrical radius ($R_{c,geo}$) of A1, A7 and A19. The $R_{c,SES}$ and $R_{c,MD}$ are the mean values taken from 1500 to 2700 K, and the error bars represent one standard deviation.

increases with the PAH size as expected. The $R_{c,SES}$ and $R_{c,geo}$ values are also mapped in Fig. 3c. It is clear that the computed $R_{c,SES}$ and $R_{c,MD}$ values are very close; $R_{c,SES}$ overestimates the collision radius by $\sim$0.5 Å in the worst case, *i.e.*, A19. In contrast, $R_{c,geo}$ always exceeds the collision radius by at least 1 Å, and the maximum deviation is seen in A19 as 2.5 Å. The collision radius of the PAH monomers can be well captured using $R_{c,SES}$ without detailed MD trajectories.

The potential reaction dynamics between the PAH monomer and H atom were then discussed in detail. Two types of reactions were observed, including the hydrogen abstraction (HB) reactions and hydrogen addition (HD) reactions. In an HB reaction, an H atom is abstracted from a PAH molecule by the incident H to form a H_2 molecule as the product, which plays an important role in the processes of PAH growth and soot formation. In an HD reaction, the incident H atom directly bonds with a C atom on a PAH. Compared with HB reactions, the HD reaction is less studied in the field of soot, but it is common in the interstellar PAHs of astrochemistry,[42] where the temperature is much lower than that of sooting flames. Fig. 4a shows the probability (P_{HB}) of the HB reactions as a function of temperature for A1, A7 and A19. For all PAH molecules, P_{HB} increases monotonically with temperature as expected in Fig. 4a. HB reactions occur more easily on the smaller PAH; the A1 molecule yields the highest P_{HB} as 0.023 at 2700 K, while the P_{HB} of the A19 molecule is only 0.009. This can be attributed to the surface properties that a larger PAH molecule has a lower α_H, leading to a lower reaction probability.

The corresponding reaction rate constants calculated from eqn (3) are also listed in Fig. 4b. At high temperature cases ($>$2100 K), A1, A7 and A19 share similar reaction constants, while A19 yields lower reaction constants by 50% at temperatures lower than 2300 K compared to both A1 and A7. These inconsistent rate constants between the small and large PAHs raise a critical argument on whether the rate constants extracted from small PAHs can be used for large ones. Our results in Fig. 4b provide a failure of the above argument. The accurate rate constants of the HB reactions on the A1 molecules are estimated from TST calculations in previous works, for example, Hou *et al.*,[7] Liu *et al.*[8] and Semenikhin *et al.*[9] In general, our predicted rate constants of A1 from the QCT method are in line with that of Liu *et al.*[8] at the CBS-QB3 level of theory, except the higher ones at 1500–1900 K. Hou *et al.*[7] estimated the HB rate constants of A1 from the M06-2X/6-311G(d,p) method, which was benchmarked against the CCSD(T)/CBS level of theory. The results of Semenikhin *et al.*[9] are calculated at the G3(MP2,CC) level of theory, which are almost the same as the nominal values of Hou *et al.*[7] Our QCT

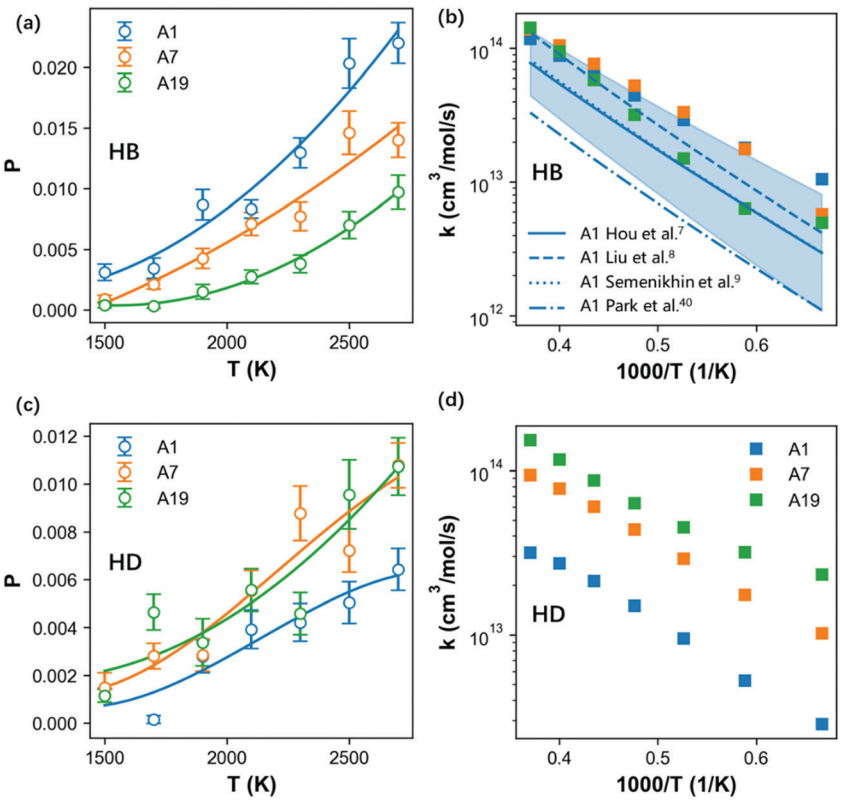

Fig. 4 Reaction probabilities of (a) hydrogen abstraction and (c) hydrogen addition for A1, A7 and A19 from 1500 to 2700 K, and the corresponding rate constants for (b) hydrogen abstraction and (d) hydrogen addition. The curves are fitted using a polynomial function. The rate constants are extracted from the fitted curves. The shadow region in (b) represents the errors estimated at the M06-2X/6-311G(d,p) level of theory.[7] The dashed curve in (b) represents the rate constants taken from the CBS-QB3 level of theory.[8] The dotted curve in (b) represents the rate constants taken from the G3(MP2,CC) level of theory.[9] The dashed-dotted curve in (b) represents the rate constants taken from the mass-spectrometric measurements.[43]

results are close to the upper bound of Hou *et al.*,[7] considering the uncertainties (*i.e.*, shadow region). The rate constants from mass-spectrometric measurements by Park *et al.*[43] are also plotted in Fig. 4b. When compared with the rates by DFT and QCT methods, the experimental measurement seems to underestimate the rates of the HB reaction. Again, at 1500–1900 K, QCT overestimates the rate constants by 50%.

The trend of the HD reactions does not follow that of the HB reactions. In Fig. 4c, the HD reaction probabilities (P_{HD}) of A7 and A19 are about 2 times larger than that of A1. Although an A19 molecule has more edge carbons for potential addition reactions, its P_{HD} are not higher than that of A7. Because not all edge carbons could react with the incident H atom. The effect of the site type will be discussed in the latter section. It should be noted that the slope of P_{HD} gradually decreases as the temperature approaches 2700 K in the case of A1. In a recent study of the ring polymer molecular dynamics for H sticking on the graphene surface,[44] it was found that the sticking probabilities of the H atom drops at high incident kinetic energies. In other words, P_{HD} does not increase monotonically with the incident kinetic energy, but decreases after reaching a critical one. This phenomenon is also observed in other systems.[45,46] For example, Valentini *et al.*[46] reported that the sticking probability of O_2 on the Pt(111) surface reaches its local maximum with a critical incident kinetic energy (E_i) as 0.4 eV. When $E_i > 0.4$ eV, the sticking probability of O_2 begins to decrease because O_2 can easily escape from the chemisorbed state (−0.25 eV). The critical kinetic energy is affected by the local potential energy surface and the energy transfer in the collision. In this work, the P_{HD} of A1 remains monotonical until 2700 K. For larger PAHs, the interaction becomes stronger, causing an increase in the critical kinetic energy. As a result, the critical incident kinetic energy increases with PAH size.

Fig. 4d presents the rate constants of HD reactions on A1, A7 and A19; clearly, the reaction constant is proportional to the PAH size. More importantly, it was found that the rate constants of the HD reactions on A19 are comparable with those of the HB reactions, for example, the rate constant of the HD reaction on A19 is three times larger than that of the HB reactions at 1900 K. In contrast, A1 undergoes slower HD reactions, and at 1900 K, the ratio between the HD reactions and HB reactions is 0.31. The channel of the HD reactions might be largely underestimated in the community due to the knowledge derived from the small PAHs (*i.e.*, A1), and the above observation highlights the significance of the direct estimation of rate constants from large PAHs.

Next, we compared the HB and HD reaction probabilities between an H atom and quasi-surface models, *i.e.*, A7s and A19s. The P_{HB} of A7s and A19s (Fig. 5a) shows minor differences except at high temperatures, suggesting that the PAH size has little effect on the reaction probability of the quasi-surface. This observation is expected due to the similar potential energy

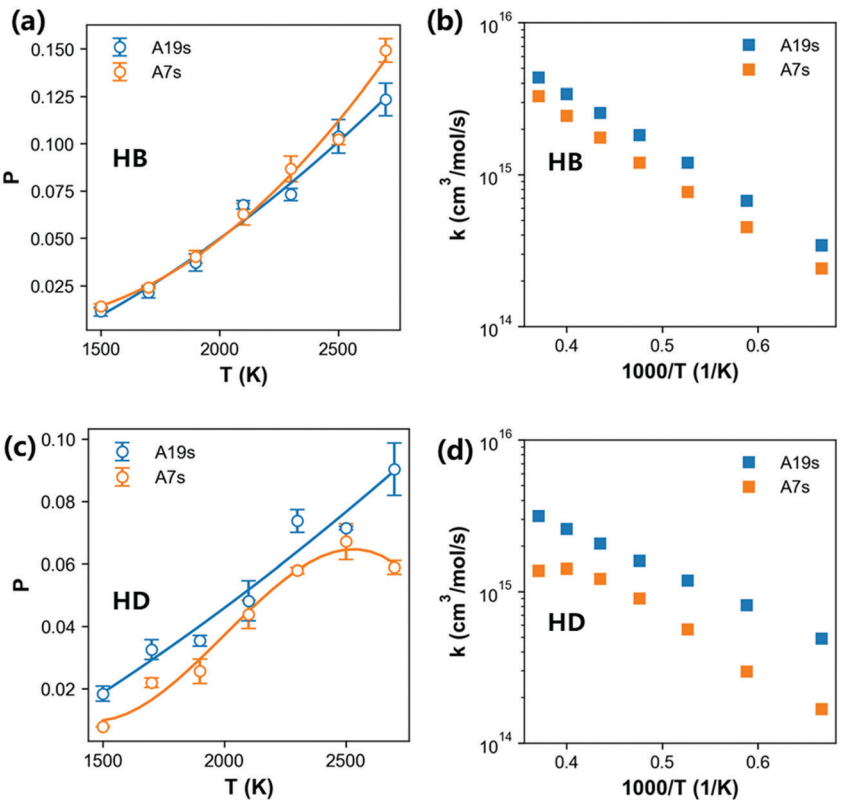

Fig. 5 Surface reaction probabilities of the (a) hydrogen abstraction and (c) hydrogen addition for A7s and A19s from 1500 to 2700 K, and the corresponding rate constants for the (b) hydrogen abstraction and (d) hydrogen addition. The curves are fitted using a polynomial function. The rate constants are extracted from the fitted curves.

surface of A7s and A19s. The overall rate constants of the HB reactions are shown in Fig. 5b; the rate constants of A19s are about 1.5 times higher than those of A7s due to the larger collision cross section. Also, the slopes of the rate constant curves are similar for these two cases. It is thus learnt that the collision cross section plays a more significant role in the HB reaction compared to the type of PAHs. In Fig. 5c, the P_{HD} of A7s shows a similar trend compared with the reactions among the A1 monomers, and the P_{HD} values reach its maximum at 2500 K. As discussed in Fig. 4c, the P_{HD} decreases after reaching the critical incident kinetic energy (or temperature), and the critical incident kinetic energy increases with PAH size. As a result, the HD rate constant of A7s shows an obvious drop at high temperatures. Below 2500 K, the difference in P_{HD} between A19s and A7s is limited. Again, the HD rate constants of A19s are 2–3 times larger than those of A7s. It should be noted that the quasi-surface model prefers abstraction reactions, as the rate constants of the HB reaction are larger than those of the HD reactions in most cases. In other words, the abstraction reaction prevails in surface reactions, unlike gas-phase reactions.

3.3 Site effect

The overall reaction kinetics of both HB and HD reactions are decomposed into reactions on each type of reactive sites. The atoms on the PAH monomers and quasi-surface models are classified into three site types, *i.e.*, inner, zig-zag (ZZ) and free-edge (FE) site (Fig. 6b). The inner atoms cannot react with the H atoms at 1500–2700 K, and thus they are excluded from our discussion here. In Fig. 6a and b, the site types on the A7 and A19 monomers are highlighted; both A7 and A19 monomers have 12 FE sites, while the A19 monomer also includes 6 ZZ sites. In the quasi-surface models, the available sites depend on the local geometry. The reactive sites are further marked by their relative positions to the neighboring molecule in Fig. 6c and d. The corresponding SES area of each site is reported for the monomers and quasi-surface models. In Fig. 6e, it was found that the surface areas of the H atoms in the most FE sites are in the range of 8.26–8.96 Å^2. However, atoms in the FE-1 sites barely contribute to the surface area ($\sim$1.0 Å^2) due to the hindrance effect. H atoms in the ZZ sites occupy a similar surface area, regardless of its relative position to the neighboring molecules. It is interesting to note that the surface area of the carbon in the monomers is about 4 times larger than that of the carbon in the quasi-surface models. This is consistent with the indication of α_H (Table 1), as the quasi-surface model is dominated by hydrogen atoms.

The incident angle of the H atoms is a critical parameter determining the fate of collision. The sampled angles of the incident velocities are in the range of 0–180°, as discussed in the previous section. In Fig. 7, the incident angle governs the accessibility of the surface sites in the first collision event, considering the weak van der Waals potential (Fig. 1). In particular, the available incident angle of the FE-3 site is up to 145°, while the accessibility of the ZZ-1 site is limited as the available incident angle is about 54°. Here, the FE-3 and ZZ-2 sites are termed as "flat sites", which sit on the edge of the quasi-surfaces, allowing a wide range of incident angles. In contrast, the FE-1, FE-2 and ZZ-1 sites are considered as "pocket sites", which has limited accessibility for the gaseous species due to the geometry hindrance. The definition of pocket sites here is in line with the previous work.[17] It was assumed that the pocket sites cannot be accessed by the gaseous species, and thus they were treated as unreactive sites. In this work, it would be interesting to resolve the question of whether the reactive sites in the pocket are accessible in collision events.

The QCT trajectories were further examined to count the numbers of collisions and reactions on each site type. For each case, the trajectories over all temperature ranges were analyzed (42 000 for each PAH monomer and 21 000 for each quasi-surface model). The results presented here refer to the per-site basis. The cases of the A1 and A7 monomers are not included because they only have FE sites. $N_{col,1st}$ represents the count of the collision events in which the incident H first

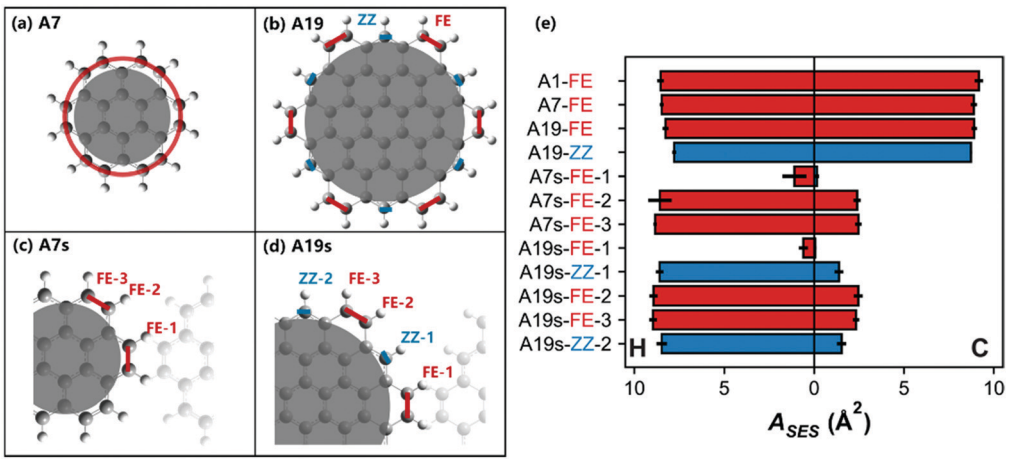

Fig. 6 (a–d) The illustrations of the site types in A7, A19, A7s and A19s. The red and blue lines represent the free-edge site, and zig-zag site, respectively. The grey transparent region represents the inner C atoms. (e) The solvent-excluded surface area (A_{SES}) of the hydrogen and carbon atoms in all sites. The error bars are extracted from the equilibrated trajectories of 10 ps to present one standard deviation.

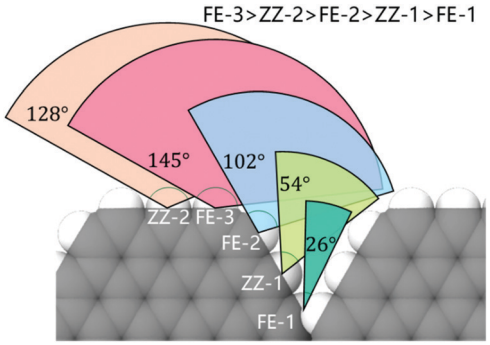

Fig. 7 Illustration of the available incident angles for each site on the A19s surface. The snapshot is taken from the y–z plane.

collides with the H and C atoms on a particular reactive site (Fig. 8a–c). It should be noted that each reactive site is composed of one H atom and one C atom, and the incident H could access both C and H atoms during the first collision due to the incident kinetic energy. Fig. 8(a–c) shows that the surface H atoms and C atoms have roughly equal probability to collide in the first collision despite the difference in the surface area (Fig. 6e). For the A19 monomers, the $N_{col,1st}$ on the H atoms of the FE site exceeds that of the ZZ site by $\sim$16%, which is consistent with the small difference in the surface area between the two sites. For quasi-surface models, the $N_{col,1st}$ of the FE-1 site is much lower than that of other FE sites, which is 4.1 and 2.0 for A7s and A19s, respectively. These small values are expected, considering their negligible contribution in the surface area (Fig. 6e) and the incident angle (Fig. 7). Taking a closer look at the comparison between the FE-2 and FE-3 sites, the $N_{col,1st}$ values of the H atoms on the FE-3 site is $\sim$60% larger than of the FE-2 site, highlighting the effect of the incident angle, even though their A_{SES} values are the same. The above cases indicate the significance of the surface area and incident angle in the determination of the overall collision rate.

After the first collision, the incident H atom might be absorbed on the particle surface and visit other sites. In Fig. 8(d–f), the total number of collisions accessed by the incident H atom within a trajectory was termed as $N_{col,all}$ for each site type. For the surface H atoms, the $N_{col,all}$ of the PAH monomer and quasi-surface models is at least 40% and 170% larger than the corresponding $N_{col,1st}$, respectively. In particular, the ratio of $N_{col,all}/N_{col,1st}$ is up to 31 for the FE-1 site on A19s, and this highlights the local accumulation of the incident H atoms into the surface pocket. A similar trend is observed from the surface C atoms as well.

In the classical gas-kinetic theory, the collision modes are classified into specular and diffusive scattering, accounting for the momentum transfer.[47–49] It is well accepted that gaseous bimolecular reactions undergo a single collision leading to the product, and the unsuccessful collision results in specular scattering. This underlying assumption underpins the majority of combustion kinetics in gaseous bimolecular reactions,[50–53] and is further extrapolated in the treatment of the surface reactions to an extent. However, the gas-nanoparticle scattering could exhibit a diffusive mode in which the gas molecule is trapped on the particle surface due to the energy accommodation of the nanoparticle. In previous works, the impact of the diffusive scattering (termed as "surface diffusion" here) is well examined in terms of the transport properties of the nanoparticles,[54] but its potential effect on the surface reactions is largely neglected in the treatment of surface models.[6,55] To examine the potential impact of the surface diffusion on the reactions, we define the number of reactions occurring on each site as N_{reax}. Fig. 9 compares the correlation among $N_{col,1st}$, $N_{col,all}$ and N_{reax}. It should be noted that $N_{col,all}$ has a better linear correlation with N_{reax}. This suggests that the first collided sites do not determine the overall reaction rate. We believe that the incident H atom can bounce on the surface

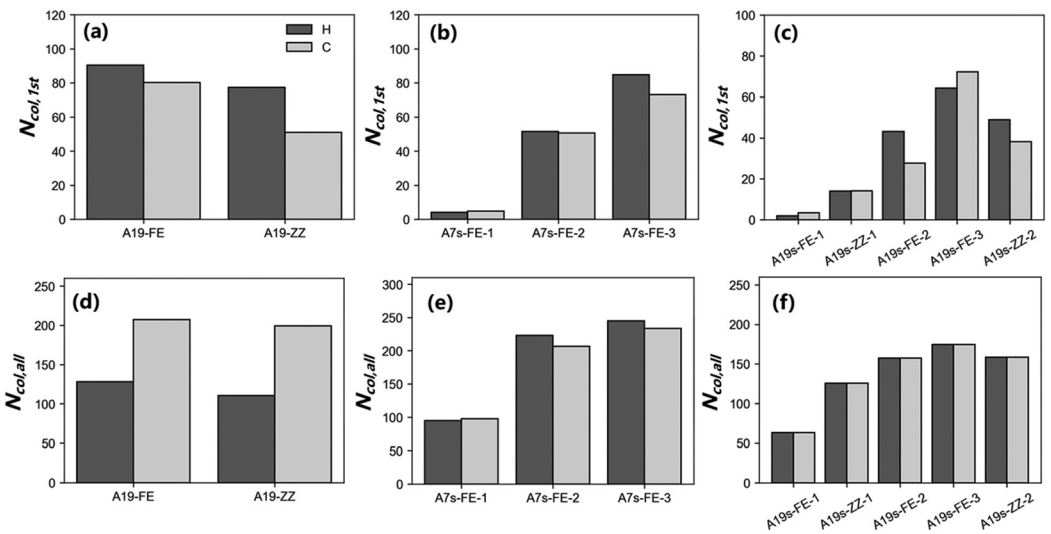

Fig. 8 Numbers of collisions of each reactive site in the first collision event between the incident H atom and surface atoms on (a) A19, (b) A7s and (c) A19s. Numbers of collisions of each reactive site during the whole trajectory for the cases of (d) A19, (e) A7s and (f) A19s. Numbers of collisions on the H and C atoms are represented by dark-grey and light-grey, respectively.

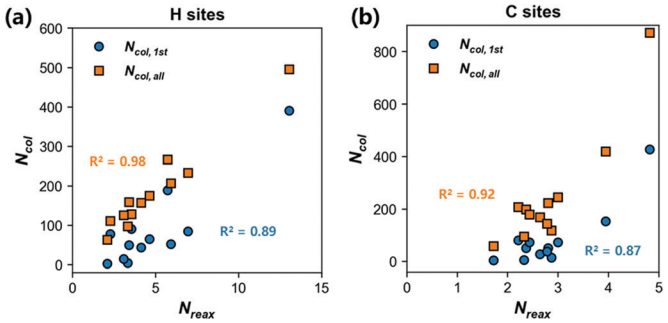

Fig. 9 The correlation between the number of collisions and N_{reax} for A1, A7, A19, A7s and A19s. Reactions on 12 types of sites are condiered here (Fig. 6a–d). The blue and yellow dots represent $N_{col,1st}$ and $N_{col,all}$, respectively. The statistics are taken from all sites in Fig. 8. The correlation coefficients (R^2) between N_{reax} and $N_{col,1st}$, and N_{reax} and $N_{col,all}$ are also marked in the figure.

and react on the reactive sites, rather than the first collided site. This phenomenon will be addressed in a later context.

The per-site rate constants of the HB and HD reactions on each site are presented in Fig. 10. All sites are divided into four sub-groups, *i.e.*, surface FE, surface ZZ, surface FE (pocket) and sites in the PAH monomers, following the magnitude of the rate constants of the HB reactions. The rate constants of a particular site overlap with other sites in each sub-group. The per-site rate constants of the HB reactions in the monomers are compared with those at the CBS-QB3 level of theory.[8] The overall rate constants from ref. 8 are converted to per-site rate constants by dividing the numbers of sites. The trend of the FE sites on A1 is discussed in Fig. 4, which is not further elaborated here. As shown in Fig. 10a, the rate constants of the HB reaction decrease with PAH size in the range of A1, A7 and A19. The FE sites show higher reactivity than the ZZ sites for HB reactions, *e.g.*, the rate constants of the HB reactions on the FE sites are ~0.8 times higher than those on the ZZ sites at 2100 K. Liu *et al.*[8] also included the reduced rate constant in phenanthrene (A3) compared to that in A1. This is consistent with our results, in which the rate constant of the HB reactions is inversely proportional to the PAH size to some extent. Considering the site effect, the rate constants of the P3-CS1 site (similar to the FE site in this paper) on A3 is ~20% larger than those of the P4-CS1 site (similar to the ZZ site in this paper).[8] Again, this is in line with our prediction that the free edge exhibits higher reactivity for HB reactions.

Fig. 10 includes all rate constants on each site in this work. The first three sub-groups include sites on the quasi-surface, and the last group refers to the sites in the PAH monomers. It is noticed that the sites in the quasi-surface models have much higher reaction rates for HB reactions than the sites in the PAH monomers, considering the impact of the surface diffusion. For example, the rate constants on the A19s-FE-2 sites are almost one order of magnitude higher than those on the A19-FE sites. The rate constants (Fig. 10a) of the FE-2 and FE-3 sites are nearly identical on both quasi-surface models. This can be attributed to the balance of the available incident angle and the local potential energy surface; the reactive sites in the flat region (FE-3) have better exposure to the gaseous species, that is, larger A_{SAS} and available incident angle, while the FE-2 sites sit next to the pocket region and exhibit a stronger local attraction. Regardless of the impact of stronger attraction, the rate constants of the FE-1 sites are ~2.3 times lower than those of FE-2 and FE-3 on average due to the minimal A_{SES}. This supports the previous assumption[17] that the reactive sites in the pocket yield reduced rates due to geometry hindrance. The rates of the HD reactions on the quasi-surface are also enhanced *via* the event of surface diffusion (Fig. 10b). Unlike HB reactions, HD reactions prefer surface ZZ sites rather than surface FE sites by a factor of 1.81 at 1900 K.

Table 2 summarizes all per-site rate constants in Arrhenius expressions recommended for kinetic models. We fitted the reaction constants of the three sub-groups of sites, including the surface FE, surface FE (pocket) and surface ZZ. For the first two sub-groups, the activation energies are the same, but the pre-exponential factor of the surface FE sites is ~2.3 times that of the FE sites at the pocket, highlighting their limited accessibility. The rate constants of the surface HB reactions calculated by the TST method from Hou *et al.*[7] and Liu *et al.*[8] are also listed in Table 2 for reference. The activation energies

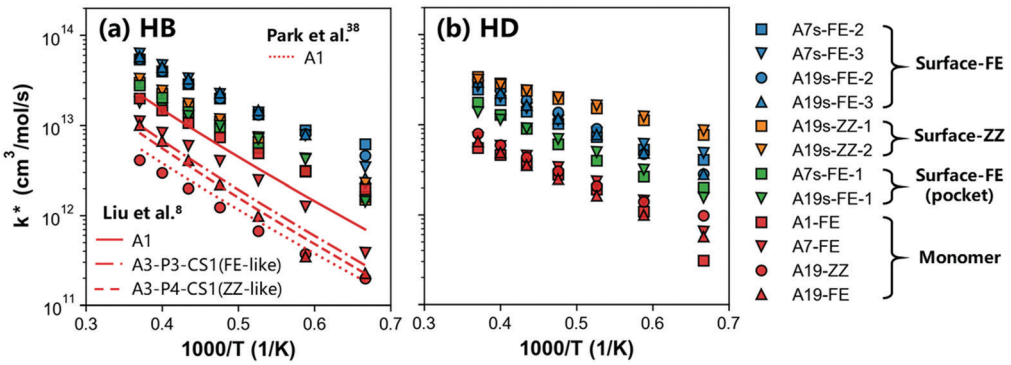

Fig. 10 Site-specific rate constants of the (a) hydrogen abstraction and (b) hydrogen addition reactions on the PAH monomers and quasi-surfaces. Four groups of sites, that is, the surface-FE, surface-ZZ, surface-FE (pocket) and sites in the PAH monomers are represented by blue, orange, green and red markers, respectively. The rate constants of A1-FE, A3-P3-CS1 and A3-P4-CS1 calculated by Liu *et al.*[8] are also represented by a solid line, dash line and dash-dot line, respectively.

Table 2 Per-site rate constants for hydrogen abstraction and addition reactions on the surface[a]

	HB		HD	
Site type	A (cm^3 mol^{-1} s^{-1})	E_a (kcal mol^{-1})	A (cm^3 mol^{-1} s^{-1})	E_a (kcal mol^{-1})
Surface-FE	2.0×10^{15}	17.70	$3.03 \times 10^6 \times T^{2.204}$	5.94
Surface-FE (pocket)	8.6×10^{14}	17.80	$2.04 \times 10^4 \times T^{2.719}$	3.97
Surface-ZZ	1.5×10^{15}	19.20	$1.44 \times 10^6 \times T^{2.292}$	5.61
A1-FE	3.4×10^{14}	15.70	$4.89 \times 10^6 \times T^{1.891}$	5.42
Surface[b]	$4.67 \times 10^9 \times T^{1.656}$	16.50	—	—
A1-FE[b]	$5.38 \times 10^9 \times T^{1.582}$	15.67	—	—
A1-FE[c]	$6.75 \times 10^8 \times T^{1.910}$	15.61	—	—
A1-FE[d]	—	—	4.03×10^{13}	4.31

[a] The rate constants in this work are fitted into the expression of $k = AT^n \exp(E_a/RT)$. [b] Rate constants of HB reactions are taken from Hou *et al.*[7] [c] Rate constants of HB reactions are taken from Liu *et al.*[8] [d] Rate constants of HD reactions are taken from Nicovich and Ravishankara.[56]

of HD reactions are in the range of 3.97 to 5.94 kcal mol^{-1}, which agree with the values of 4.31 kcal mol^{-1} from Nicovich and Ravishankara.[56]

3.4 Surface diffusion

The impact of the surface diffusion on the overall reaction rate was further investigated to reveal the full image of reaction dynamics of the H atoms on PAHs. Fig. 11a illustrates an example in which the incident H atom undergoes an HB reaction after the third collision on the pocket sites of the particle surface. A similar example for the HD reaction is also included in Fig. 11a. The above two cases involve two reactions *via* surface diffusion, and we term this type of surface reactions as a surface diffusion-induced reaction. The number of sites that an incident H atom visits in each trajectory (N_{site}) and its distribution for all five models are illustrated in Fig. 11b. Each row represents the distribution of N_{site} for a particular case from 1500 to 2700 K, and the median value of N_{site} is marked by white dots. For PAH monomers, the median values of N_{site} are 1 and 2–3 for the surface H and C atoms, respectively. This is consistent with the finding in Fig. 8, as the incident H atom can access both H and C atoms at the same time in a single collision event. The N_{site} of the PAH monomers suggests that the incident H atom only visits the surface H atom once in one trajectory, but multiple times for surface C atoms. However, considering the overlap of the surface C atoms, the incident H atom in fact collides on more than one C atom at the same time, resulting in the N_{site} of the C atom exceeding one. Therefore, the collisions between the incident H atoms and PAH monomers are governed by the specular scattering, as expected. The distributions of the N_{site} for the PAH monomers have a long tail toward tens of visited sites, indicating that surface diffusion exists in the bimolecular collision to an extent. A larger PAH shows a longer tail, which is consistent with the ability of momentum accommodation.[57] For the quasi-surface models, both N_{site} values of the C and H sites are higher than that of monomers on average, suggesting that diffusive scattering dominates the interactions between the incident H and surface atoms.

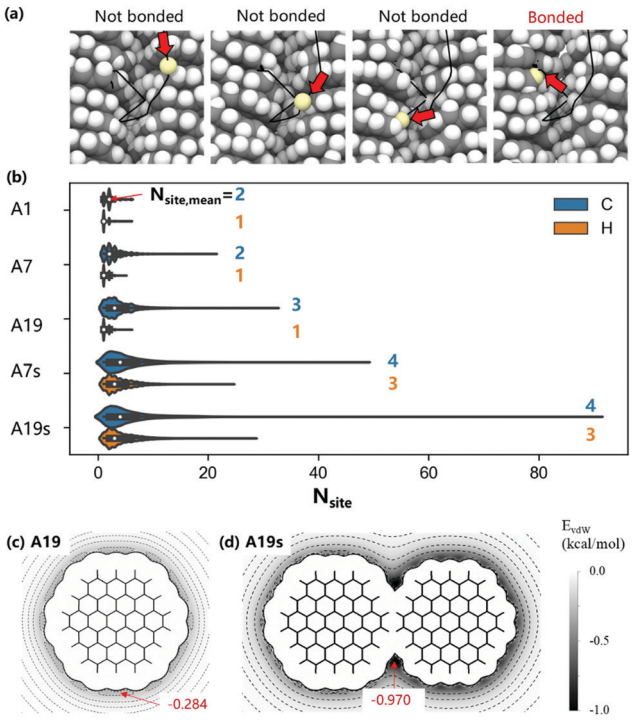

Fig. 11 (a) Snapshots of trajectories for surface diffusion-induced HB and HD reactions on A19s. (b) The number of C and H atoms visited by the incident H atom after the collisions on the surface H atom. The shadow regions represent the detailed distribution. The white dots represent the median values, which are also highlighted on the right side of the figure. The van der Waals potential energy surface of (c) A19 and (d) A19s. The cross section of the A19s is cut through the plane of the left A19 molecule. The minimum potential energies are highlighted by the red values.

We also learned that the N_{site} is almost independent of the temperature (Fig. S10, ESI†). However, this does not agree with the previous understanding of gas-nanoparticle scattering,[54] as the kinetic energy of the incident atoms impacts the scattering mode. This might be attributed to the good ability of the energy accommodation in PAH molecules. To understand the discrepancy between the surface diffusion on PAH monomers and quasi-surfaces, the van der Waals potential energy surfaces of A19 and A19s were constructed following the method of Lu and Chen,[58] and visualized using the Multiwfn program.[59] An H atom was used as a probe to calculate the potential energy surface. A negative potential energy (*i.e.*, E_{vdw}) indicates that the incident H atom is attracted by the neighboring atoms. The average incident kinetic energies of the H atoms are in the range

of 4–8 kcal mol^{-1} at 1500–2700 K, which are comparable with the van der Waals potential on the particle surface. It is expected that the incident H atoms exhibit weak attractions from the surface atoms before collision. As shown in Fig. 11c and d, the E_{vdw} values of A19s are larger than that of A19 (absolute value), suggesting that the attractions in the quasi-surface models are stronger. The spatial distribution of E_{vdw} for A19 is uniform, while the pocket sites of the quasi-surface models show a larger E_{vdw} by ~0.5 kcal mol^{-1} compared to the flat regions, and this supports the enhancement of collisions in the pocket sites (Fig. 8).

The representative collision dynamics of the surface diffusion-induced reactions is illustrated from the kinetic energy of the incident H atom on the surface of A19s (Fig. 12). In the first trajectory (Fig. 12a), the incident H atom undergoes a diffusive scattering. It gains ~5 kcal mol^{-1} in the first collision at ~260 ps, and then experiences multiple collisions to gain and lose kinetic energy. Finally, it gains ~9 kcal mol^{-1} from the last collision (~1460 fs) to overcome the surface attraction (Fig. 11d), resulting in the desorption from the surface. It should be noted that the kinetic energy exhibits a minor fluctuation during the surface diffusion. In Fig. 12b, the evolution of the kinetic energy of an HB reaction is presented, where the incident H atom reacts with the surface H atom to release a H_2 molecule. The incident H atom collides with the surface at 510 fs and loses ~4 kcal mol^{-1} in the first collision. It further undergoes surface diffusion on the surface of A19s, which involves 12 collisions in total. After the last collision at ~2180 fs, the kinetic energy of the incident H atom reaches up to 20 kcal mol^{-1}, which overcomes the energy barrier of the HB reactions (~16.5 kcal mol^{-1}),[7] and an HB reaction occurs. Similarly, the acceleration of the H atom during the surface diffusion can lead to an HD reaction as well (Fig. 12c).

The nature of surface diffusion-induced reactions lies in the energy transfer between the incident species and surface atoms. Once the incident species gains enough kinetic energy from surface diffusion, the potential surface reaction could be seen afterward. The previous knowledge neglects the potential reactions in the diffusive scattering,[54] where the incident species loses its kinetic energy and no reaction proceeds. However, our findings here demonstrate the importance of surface diffusion-induced reactions, and highlight the feasibility to gain kinetic energy from surface diffusion in the models of soot surface.

The probabilities of surface diffusion in all trajectories are discussed together with the proportions of surface diffusion-induced HB and HD reactions (Fig. 13). We selected $N_{site,H} > 2$ as a critical value to recognize the surface diffusion. The diffusive scattering only accounts for 0.91–1.44% of all collisions between the incident H and PAH monomers, while the probability of diffusive scattering is enhanced to 59.4–60.9% for quasi-surface models. Both surface diffusion-induced HB and HD reactions are insignificant (~4%) in the cases of the

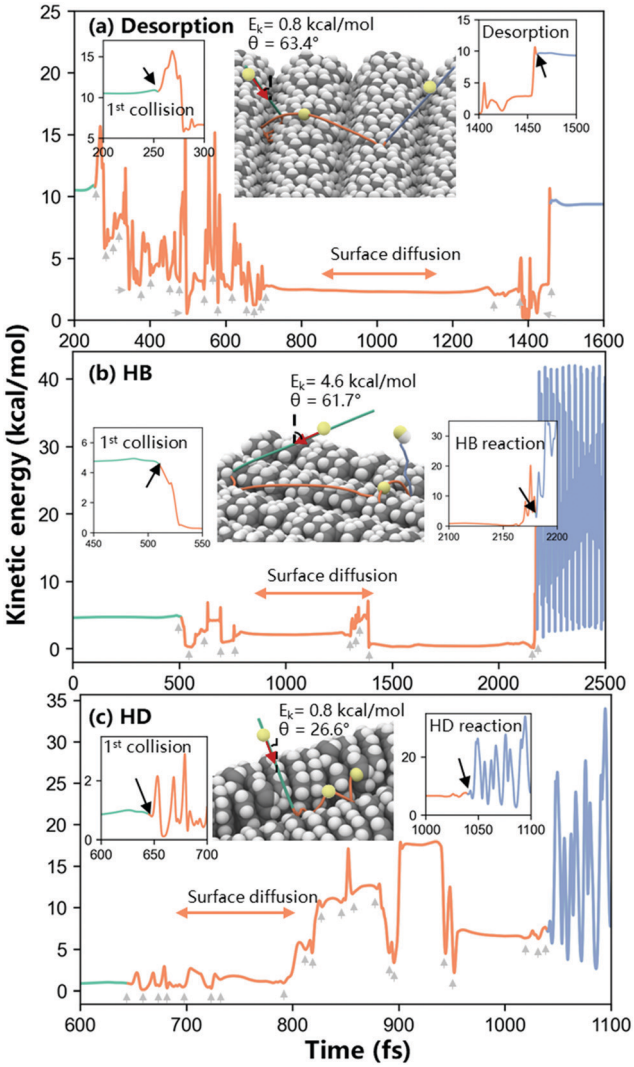

Fig. 12 Kinetic energy profiles of an incident H atom in three representative trajectories involving surface diffusion: (a) desorption after non-reactive collisions, (b) HB reaction and (c) HD reaction. The grey arrows highlight the collisions between the incident H atom and surface atoms. Detailed animations of three representative trajectories are included in the ESI.†

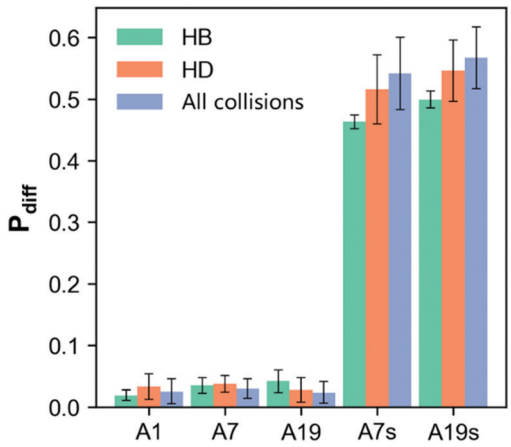

Fig. 13 The contribution of surface diffusion (P_{diff}) into the HB reactions, HD reactions and all collisions for cases of A1, A7, A19, A7s and A19s. The green, orange and blue bars represent the P_{diff} in HB reactions, HD reactions and all collision events, respectively. The error bars are one standard deviation computed by the bootstrapping resampling method.

PAH monomers as expected, and the reactions can be approximated as the product of a single collision. In contrast, ~50% of both HB and HD reactions proceed *via* multiple collisions between the incident H atom and surface atoms, that is, surface diffusion-induced reactions. This proves that the surface diffusion-induced reactions are critical in the treatment of surface reactions in soot formation. However, the surface diffusion-induced reactions were not novel in surface science, and they were previously observed in the area of metal catalysis, for example, the Langmuir–Hinshelwood (LH) mechanism. In the LH mechanism, two reacting species are chemisorbed on the catalyst surface, and the surface diffusion events drive the two species together before a reaction takes place.[60] Examples of the LH mechanism are seen in the systems of H + H-absorbed Ni(100),[61] H + Cl-adsorbed Au(111),[62] and H + H-absorbed graphite.[63] A similar concept termed as the ''mobile precursor mechanism'' is available in the soot community, where the multiple collisional events between the gaseous reactants offer the opportunity for a reaction to take place.[64] Recently, Frenklach and Mebel invoke this concept to explore the mechanisms of soot particle nucleation.[24] They proposed a new reaction termed ''E-bridge'', where a rotationally-activated dimer is formed in a collision of an aromatic molecule and an aromatic radical; and the two species experience repeated edge bumping during the lifetime of the rotationally-activated dimer. Furthermore, Semenikhin *et al.*[25] recently proposed that a new model combining rotationally-induced formations of E-bridges successfully reaches the level of nucleation fluxes comparable to those of the irreversible dimerization models, and the latter models have been shown to reproduce soot inception in flames.[65,66] The above discussion shows that the phenomenon of surface diffusion or mobile precursor mechanism (rotationally-induced formation of E-bridges) can significantly affect the reaction dynamics in gas-particle and large molecule systems. Therefore, the impact of surface diffusion on the surface reactions of soot should not be neglected, and further detailed analysis will help the development of surface reaction models.

Soot particles have complex surface structures, including cross-linking,[67] heteroatoms[68] and curved PAHs,[69] and the current model focuses on a series of simplified quasi-surface models that only involves C–H sites. However, we believe that the surface diffusion-induced reactions exist in other cases. When the surface evolves to carbon-rich configurations as the soot becomes mature, the preferred reaction pathway might be switched from HB reactions to HD reactions. The HD reactions could superhydrogenate the particle surface, which would weaken the C-backbone and accelerate the fragmentation upon collisions or photoionization.[70,71] A further study on the fate of the product of HD reactions is critical to assess its impact on the surface reactions. The products of HD reactions are not thermally stable under flame conditions; H loss dominates and H addition complexes do not survive long enough to enter further reactions.[24] Our current study resolves the collision dynamics of the H radical and PAHs, and further investigation of the dissociation channel will be required in a future work. Besides H atoms, other radical species, *i.e.*, OH and CH_3, also play an important role in the PAH chemistry. A competition between the abstraction and addition reactions among these species is expected, and the rate of each reaction pathway depends on the local potential energy surface.

4. Conclusions

The quasi-classical trajectories (QCT) method in combination with molecular geometric analysis are applied to explore the HB and HD reactions on PAH monomers and quasi-surface models from 1500 to 2700 K. The molecular structures of the monomers and quasi-surface models are investigated by solvent-excluded surface (SES) area. For PAH monomers, it was found that the percentage of surface hydrogen atom (α_H) decreases with the PAH size, resulting in the preferred reaction pathway changing from HB to HD reactions. In contrast, the quasi-surface models exhibit weak dependence on the PAH size due to the similar α_H. Furthermore, several reactive sites are highlighted to understand the effects of the surface area, incident angle and van der Waals potential on the reaction dynamics. We observed the phenomenon of the surface diffusion in the models of quasi-surface, where the incident H atom collides with several reactive sites. A portion of the surface diffusion results in the HB or HD reactions on the particle surface due to the gain of kinetic energy from the surface atoms. This type of unexpected reactions prevails in the models of the quasi-surface sites, resulting in one order of magnitude enhancement of the reaction rates compared to those of the monomer sites at the maximum.

Our study also highlights the misuse of small PAHs to represent the large PAHs or even soot particles for considering the underlying reaction kinetics, which might underestimate the magnitudes of surface reaction rates and misinterpret the reaction path in the worst cases. The key lies in the treatment of surface diffusion-induced reactions. More future studies are required to determine the intensity of the surface diffusion and its impact on the reaction pathway among more complex surfaces (involving C rich, cross-linking, curved PAH) and gas species (OH and CH_3). However, the surface diffusion phenomena should always exist on the particle surface, and become stronger as the particle size increases. We anticipate that the surface reactions in the events of the surface diffusion discovered here apply to other gas-surface reactions, which is of critical significance for our understanding of chemical reactions in surface reactions. It should be noted that the reverse reaction can affect the PAH and soot growth, *e.g.*, H addition to the radical formed by the H abstraction, which will be accelerated by the surface diffusion as well. Therefore, further study on the reverse reaction is needed to understand the dynamics of the soot surface reaction. Also, we expect that our results can stimulate the development of experimental methods to explore such unexpected phenomena from the basis of reaction kinetics in soot formation.

Conflicts of interest

There are no conflicts to declare.

Acknowledgements

This work was supported by the National Natural Science Foundation of China (Grant No. 21961122007, 51806016, 11672314 and 51676016). D. C. also acknowledges the support by the Beijing Institute of Technology Research Fund Program for Young Scholars.

References

1 R. Niessner, The many faces of soot: characterization of soot nanoparticles produced by engines, *Angew. Chem., Int. Ed.*, 2014, **53**, 12366–12379, DOI: 10.1002/anie.201402812.
2 H. Wang, Formation of nascent soot and other condensed-phase materials in flames, *Proc. Combust. Inst.*, 2011, **33**, 41–67, DOI: 10.1016/j.proci.2010.09.009.
3 M. Alfè, B. Apicella, R. Barbella, J. N. Rouzaud, A. Tregrossi and A. Ciajolo, Structure-property relationship in nano-structures of young and mature soot in premixed flames, *Proc. Combust. Inst.*, 2009, **32 I**, 697–704, DOI: 10.1016/j.proci.2008.06.193.
4 R. A. Dobbins, R. A. Fletcher, B. A. Benner and S. Hoeft, Polycyclic aromatic hydrocarbons in flames, in diesel fuels, and in diesel emissions, *Combust. Flame*, 2006, **144**, 773–781, DOI: 10.1016/j.combustflame.2005.09.008.
5 J. Singh, M. Balthasar, M. Kraft and W. Wagner, Stochastic modeling of soot particle size and age distributions in laminar premixed flames, *Proc. Combust. Inst.*, 2005, **30**, 1457–1465, DOI: 10.1016/j.proci.2004.08.120.
6 M. Sander, R. I. A. Patterson, A. Braumann, A. Raj and M. Kraft, Developing the PAH-PP soot particle model using process informatics and uncertainty propagation, *Proc. Combust. Inst.*, 2011, **33**, 675–683, DOI: 10.1016/j.proci.2010.06.156.
7 D. Hou and X. You, Reaction kinetics of hydrogen abstraction from polycyclic aromatic hydrocarbons by H atoms, *Phys. Chem. Chem. Phys.*, 2017, **19**, 30772–30780, DOI: 10.1039/C7CP04964A.
8 P. Liu, Z. Li, A. Bennett, H. Lin, S. M. Sarathy and W. L. Roberts, The site effect on PAHs formation in HACA-based mass growth process, *Combust. Flame*, 2019, **199**, 54–68, DOI: 10.1016/j.combustflame.2018.10.010.
9 A. Semenikhin, A. Savchenkova, I. Chechet, S. Matveev, Z. Liu and M. Frenklach, *et al.*, Rate constants for H abstraction from benzo (a) pyrene and chrysene: a theoretical study, *Phys. Chem. Chem. Phys.*, 2017, **19**, 25401–25413.
10 M. Frenklach, New form for reduced modeling of soot oxidation: accounting for multi-site kinetics and surface reactivity, *Combust. Flame*, 2019, **201**, 148–159, DOI: 10.1016/j.combustflame.2018.12.023.
11 M. Frenklach, Reaction mechanism of soot formation in flames, *Phys. Chem. Chem. Phys.*, 2002, **4**, 2028–2037, DOI: 10.1039/b110045a.
12 M. Frenklach, On surface growth mechanism of soot particles, *Symp. (Int.) Combust., [Proc.]*, 1996, **26**, 2285–2293, DOI: 10.1016/S0082-0784(96)80056-7.
13 Q. Mao, A. C. T. van Duin and K. H. Luo, Formation of incipient soot particles from polycyclic aromatic hydrocarbons: a ReaxFF molecular dynamics study, *Carbon*, 2017, **121**, 380–388, DOI: 10.1016/j.carbon.2017.06.009.
14 T. S. Totton, A. J. Misquitta and M. Kraft, A quantitative study of the clustering of polycyclic aromatic hydrocarbons at high temperatures, *Phys. Chem. Chem. Phys.*, 2012, **14**, 4081–4094, DOI: 10.1039/c2cp23008a.
15 D. Chen, T. S. Totton, J. W. J. Akroyd, S. Mosbach and M. Kraft, Size-dependent melting of polycyclic aromatic hydrocarbon nano-clusters: a molecular dynamics study, *Carbon*, 2014, **67**, 79–91, DOI: 10.1016/j.carbon.2013.09.058.
16 D. Chen and K. H. Luo, Reactive sites on the surface of polycyclic aromatic hydrocarbon clusters: a numerical study, *Combust. Flame*, 2020, **211**, 362–373, DOI: 10.1016/j.combustflame.2019.09.034.
17 D. Chen, J. Akroyd, S. Mosbach and M. Kraft, Surface reactivity of polycyclic aromatic hydrocarbon clusters, *Proc. Combust. Inst.*, 2015, **35**, 1811–1818, DOI: 10.1016/j.proci.2014.06.140.
18 M. H. Akter *A quasiclassical trajectory study of $H_2 + H_2$ energy transfer: a survey of applicability of detailed balance. Masters,* University of Northern British Columbia, 2016, DOI: 10.24124/2016/1215.
19 Y. Zhu, L. Tian, H. Song and M. Yang, Kinetic and dynamic studies of the $H^{3+} + CO \rightarrow H^2 + HCO^+/HOC^+$ reaction on a high-level *ab initio* potential energy surface, *J. Chem. Phys.*, 2019, **151**, 054311, DOI: 10.1063/1.5110934.
20 H.-G. Yu, Product Branching Ratios of the Reaction of CO with H_3^+ and H_2D^+, *Astrophys. J.*, 2009, **706**, L52–L55, DOI: 10.1088/0004-637X/706/1/L52.
21 J. Zhao, Y. Xu, D. Yue and Q. Meng, Quasi-classical trajectory study of the reaction H + FO → OH + F, *Chem. Phys. Lett.*, 2009, 3, DOI: 10.1016/j.cplett.2009.02.007.
22 K. Song, P. de Sainte Claire, W. L. Hase and K. C. Hass, Comparison of molecular dynamics and variational transition-state-theory calculations of the rate constant for H-atom association with the diamond {111} surface, *Phys. Rev. B: Condens. Matter Mater. Phys.*, 1995, **52**, 2949–2958, DOI: 10.1103/PhysRevB.52.2949.
23 Y.-L. Fu, X. Lu, Y.-C. Han, B. Fu, D. H. Zhang and J. M. Bowman, Collision-induced and complex-mediated roaming dynamics in the $H + C_2H_4 \rightarrow H_2 + C_2H_3$ reaction, *Chem. Sci.*, 2020, **11**, 2148–2154, DOI: 10.1039/C9SC05951B.
24 M. Frenklach and A. M. Mebel, On the mechanism of soot nucleation, *Phys. Chem. Chem. Phys.*, 2020, **22**, 5314–5331, DOI: 10.1039/D0CP00116C.
25 A. S. Semenikhin, A. S. Savchenkova, I. V. Chechet, S. G. Matveev, M. Frenklach and A. M. Mebel, On the mechanism of soot nucleation. II. E-bridge formation at the PAH bay, *Phys. Chem. Chem. Phys.*, 2020, **22**, 17196–17204, DOI: 10.1039/D0CP02554B.
26 J. Happold, H.-H. Grotheer and M. Aigner, *Soot precursors consisting of stacked pericondensed PAHs*, KIT Scientific Publishing, Karlsruhe, Germany, 2009.
27 M. Commodo, K. Kaiser, G. De Falco, P. Minutolo, F. Schulz and A. D'Anna, *et al.*, On the early stages of soot formation:

molecular structure elucidation by high-resolution atomic force microscopy, *Combust. Flame*, 2019, **205**, 154–164, DOI: 10.1016/j.combustflame.2019.03.042.

28 H.-G. Yu and J. T. Muckerman, *Ab Initio* and Direct Dynamics Studies of the Reaction of Singlet Methylene with Acetylene and the Lifetime of the Cyclopropene Complex, *J. Phys. Chem. A*, 2005, **109**, 1890–1896, DOI: 10.1021/jp045049w.

29 M. R. Kholghy, A. Veshkini and M. J. Thomson, The core–shell internal nanostructure of soot – A criterion to model soot maturity, *Carbon*, 2016, **100**, 508–536, DOI: 10.1016/j.carbon.2016.01.022.

30 R. H. Hurt, G. P. Crawford and H.-S. Shim, Equilibrium nanostructure of primary soot particles, *Proc. Combust. Inst.*, 2000, **28**, 2539–2546, DOI: 10.1016/S0082-0784(00)80670-0.

31 Y. Jiang, S. Deng, S. Hong, J. Zhao, S. Huang and C.-C. Wu, *et al.*, Energetic performance of optically activated aluminum/graphene oxide composites, *ACS Nano*, 2018, **12**, 11366–11375, DOI: 10.1021/acsnano.8b06217.

32 S. Wang, G. Zhou, Y. Ma, L. Gao, R. Song and G. Jiang, *et al.*, Molecular dynamics investigation on the adsorption behaviors of H_2O, CO_2, CH_4 and N_2 gases on calcite $(1\bar{1}0)$ surface, *Appl. Surf. Sci.*, 2016, **385**, 616–621, DOI: 10.1016/j.apsusc.2016.05.026.

33 M. Sirignano, A. Collina, M. Commodo, P. Minutolo and A. D'Anna, Detection of aromatic hydrocarbons and incipient particles in an opposed-flow flame of ethylene by spectral and time-resolved laser induced emission spectroscopy, *Combust. Flame*, 2012, **159**, 1663–1669, DOI: 10.1016/j.combustflame.2011.11.005.

34 S. Plimpton, Fast parallel algorithms for short – range molecular dynamics, *J. Comput. Phys.*, 1995, **117**, 1–19, DOI: 10.1006/jcph.1995.1039.

35 Q. Mao and K. H. Luo, Trace metal assisted polycyclic aromatic hydrocarbons fragmentation, growth and soot nucleation, *Proc. Combust. Inst.*, 2019, **37**, 1023–1030, DOI: 10.1016/j.proci.2018.06.106.

36 Q. Mao, Y. Ren, K. H. Luo and A. C. T. van Duin, Dynamics and kinetics of reversible homo-molecular dimerization of polycyclic aromatic hydrocarbons, *J. Chem. Phys.*, 2017, **147**, 244305, DOI: 10.1063/1.5000534.

37 M. F. Sanner, A. J. Olson and J.-C. Spehner, Reduced surface: an efficient way to compute molecular surfaces, *Biopolymers*, 1996, **38**, 305–320, DOI: 10.1002/(SICI)1097-0282(199603)38:3<305::AID-BIP4>3.0.CO;2-Y.

38 A. Bondi, van der Waals volumes and radii, *J. Phys. Chem.*, 1964, **68**, 441–451, DOI: 10.1021/j100785a001.

39 R. Johnson, *Computational chemistry comparison and benchmark database, NIST Standard Reference Database 101*, 2002, DOI: 10.18434/T47C7Z.

40 J. Nevitt and G. R. Hancock, Performance of bootstrapping approaches to model test statistics and parameter standard error estimation in structural equation modeling, *Struct Equ Model*, 2001, **8**, 353–377, DOI: 10.1207/S15328007SEM0803_2.

41 D. Hou, D. Zong, C. S. Lindberg, M. Kraft and X. You, On the coagulation efficiency of carbonaceous nanoparticles, *J. Aerosol Sci.*, 2020, **140**, 105478, DOI: 10.1016/j.jaerosci.2019.105478.

42 N. Foley, S. Cazaux, D. Egorov, L. M. P. V. Boschman, R. Hoekstra and T. Schlatholter, Molecular hydrogen formation on interstellar PAHs through Eley-Rideal abstraction reactions, *Mon. Not. R. Astron. Soc.*, 2018, **479**, 649–656, DOI: 10.1093/mnras/sty1528.

43 J. Park, I. V. Dyakov and M. C. Lin, FTIR and Mass-spectrometric measurements of the rate constant for the $C_6H_5 + H_2$ reaction, *J. Phys. Chem. A*, 1997, **101**, 8839–8843, DOI: 10.1021/jp972162w.

44 H. Jiang, M. Kammler, F. Ding, Y. Dorenkamp, F. R. Manby and A. M. Wodtke, *et al.*, Imaging covalent bond formation by H atom scattering from graphene, *Science*, 2019, **364**, 379–382, DOI: 10.1126/science.aaw6378.

45 G. N. Seminara, I. F. Peludhero, W. Dong, A. E. Martínez and H. F. Busnengo, Molecular Dynamics study of molecular and dissociative adsorption using system-specific force fields based on *ab initio* calculations: $CO/Cu_{(110)}$ and $CH_4/Pt_{(110)}$, *Top. Catal.*, 2019, **62**, 1044–1052, DOI: 10.1007/s11244-019-01196-9.

46 P. Valentini, T. E. Schwartzentruber and I. Cozmuta, Molecular dynamics simulation of O_2 sticking on $Pt_{(111)}$ using the *ab initio* based ReaxFF reactive force field, *J. Chem. Phys.*, 2010, **133**, 084703, DOI: 10.1063/1.3469810.

47 B. E. Dahneke, Slip correction factors for nonspherical bodies—II free molecule flow, *J. Aerosol Sci.*, 1973, **4**, 147–161, DOI: 10.1016/0021-8502(73)90066-9.

48 P. S. Epstein, On the resistance experienced by spheres in their motion through gases, *Phys. Rev.*, 1924, **23**, 710, DOI: 10.1103/PhysRev.23.710.

49 R. A. Millikan, Coefficients of slip in gases and the law of reflection of molecules from the surfaces of solids and liquids, *Phys. Rev.*, 1923, **21**, 217, DOI: 10.1103/PhysRev.21.217.

50 D. Chen, K. Wang and H. Wang, Violation of collision limit in recently published reaction models, *Combust. Flame*, 2017, **186**, 208–210, DOI: 10.1016/j.combustflame.2017.08.005.

51 D. M. Golden, M. Frenklach, N. W. Moriarty, B. Eiteneer, M. Goldenberg and C. T. Bowman, *et al.*, *GRI-MECH 3.0*, 2000, http://www.me.berkeley.edu/gri_mech/.

52 H. Wang, X. You, V. J. Ameya and G. D. Scott, *USC mech Version II. high-temperature combustion reaction model of H_2/CO/C1–C4 compounds, 2007, http://ignis.usc.edu/USC_Mech_II.htm.*

53 W. K. Metcalfe, S. M. Burke, S. S. Ahmed and H. J. Curran, A Hierarchical and comparative kinetic modeling study of C1−C2 hydrocarbon and oxygenated fuels, *Int. J. Chem. Kinet.*, 2013, **45**, 638–675, DOI: 10.1002/kin.20802.

54 Z. Li and H. Wang, Gas-nanoparticle scattering: a molecular view of momentum accommodation function, *Phys. Rev. Lett.*, 2005, **95**, 014502, DOI: 10.1103/PhysRevLett.95.014502.

55 A. Raj, M. Celnik, R. Shirley, M. Sander, R. Patterson and R. West, *et al.*, A statistical approach to develop a detailed soot growth model using PAH characteristics, *Combust. Flame*, 2009, **156**, 896–913, DOI: 10.1016/j.combustflame.2009.01.005.

56 J. M. Nicovich and A. R. Ravishankara, Reaction of hydrogen atom with benzene: Kinetics and mechanism, *J. Phys. Chem.*, 1984, **88**, 2534–2541, DOI: 10.1021/j150656a021.

57 H. Wang, K. Wen, X. You, Q. Mao, K. H. Luo and M. J. Pilling, *et al.*, Energy transfer in intermolecular collisions of

polycyclic aromatic hydrocarbons with bath gases He and Ar, *J. Chem. Phys.*, 2019, **151**, 044301, DOI: 10.1063/1.5094104.

58 T. Lu and Q. Chen, van der Waals potential: an important complement to molecular electrostatic potential in studying intermolecular interactions, *J. Mol. Model.*, 2020, **26**, 315, DOI: 10.1007/s00894-020-04577-0.

59 T. Lu and F. Chen, Multiwfn: a multifunctional wavefunction analyzer, *J. Comput. Chem.*, 2012, **33**, 580–592, DOI: 10.1002/jcc.22885.

60 C. T. Rettner and D. J. Auerbach, Distinguishing the Direct and Indirect Products of a Gas-Surface Reaction, *Science*, 1994, **263**, 365–367, DOI: 10.1126/science.263.5145.365.

61 Z. B. Guvenc, X. Sha and B. Jackson The Effects of Lattice Motion on Eley-Rideal and Hot Atom Reactions: Quasiclassical Studies of Hydrogen Recombination on Ni(100) n.d.:7.

62 J. G. Quattrucci, B. Jackson and D. Lemoine, Eley–Rideal reactions of H atoms with Cl adsorbed on Au(111): quantum and quasiclassical studies, *J. Chem. Phys.*, 2003, **118**, 2357–2366, DOI: 10.1063/1.1533735.

63 R. Martinazzo and G. F. Tantardini Quantum study of Eley-Rideal reaction and collision induced desorption of hydrogen atoms on a graphite surface. I. H-chemisorbed case. J Chem Phys n.d.:15.

64 C. S. Carmer, B. Weiner and M. Frenklach, Molecular dynamics with combined quantum and empirical potentials: C_2H_2 adsorption on Si(100), *J. Chem. Phys.*, 1993, **99**, 1356–1372, DOI: 10.1063/1.465381.

65 D. Hou, C. S. Lindberg, M. Y. Manuputty, X. You and M. Kraft, Modelling soot formation in a benchmark ethylene stagnation flame with a new detailed population balance model, *Combust. Flame*, 2019, **203**, 56–71, DOI: 10.1016/j.combustflame.2019.01.035.

66 J. Appel, H. Bockhorn and M. Frenklach, Kinetic modeling of soot formation with detailed chemistry and physics: laminar premixed flames of C2 hydrocarbons, *Combust. Flame*, 2000, **121**, 122–236, DOI: 10.1016/s0010-2180(99)00135-2.

67 J. W. Martin, D. Hou, A. Menon, L. Pascazio, J. Akroyd and X. You, *et al.*, Reactivity of polycyclic aromatic hydrocarbon soot precursors: Implications of localized π-radicals on rim-based pentagonal rings, *J. Phys. Chem. C*, 2019, **123**, 26673–26682, DOI: 10.1021/acs.jpcc.9b07558.

68 K. O. Johansson, T. Dillstrom, M. Monti, F. El Gabaly, M. F. Campbell and P. E. Schrader, *et al.*, Formation and emission of large furans and oxygenated hydrocarbons from flames, *Proc. Natl. Acad. Sci. U. S. A.*, 2016, **113**, 8374–8379, DOI: 10.1073/pnas.1604772113.

69 J. W. Martin, K. Bowal, A. Menon, R. I. Slavchov, J. Akroyd and S. Mosbach, *et al.*, Polar curved polycyclic aromatic hydrocarbons in soot formation, *Proc. Combust. Inst.*, 2019, **37**, 1117–1123, DOI: 10.1016/j.proci.2018.05.046.

70 M. Gatchell, M. H. Stockett, N. de Ruette, T. Chen, L. Giacomozzi and R. F. Nascimento, *et al.*, Failure of hydrogenation in protecting polycyclic aromatic hydrocarbons from fragmentation, *Phys. Rev. A: At., Mol., Opt. Phys.*, 2015, **92**, 050702, DOI: 10.1103/PhysRevA.92.050702.

71 M. Wolf, L. Giacomozzi, M. Gatchell, N. de Ruette, M. H. Stockett and H. T. Schmidt, *et al.*, Hydrogenated pyrene: statistical single-carbon loss below the knockout threshold, *Eur. Phys. J. D.*, 2016, **70**, 85, DOI: 10.1140/epjd/e2016-60735-3.

